Numerical Treatment of Cross-Shelf Open Boundaries in a Barotropic Coastal Ocean Model

DAVID C. CHAPMAN

Woods Hole Oceanographic Institution, Woods Hole, MA 02543*

(Manuscript received 7 January 1985, in final form 2 April 1985)

ABSTRACT

Using a barotropic coastal ocean model with a straight coastline and uniform cross-shelf bottom slope, seven different cross-shelf open boundary conditions (four of which are applied in either implicit or explicit form) are compared in three numerical experiments. 1) A mound of water is allowed to collapse and radiate waves toward the open boundaries. 2) A uniform alongshelf wind stress is applied at zero time over the entire shelf and held constant for the duration of the experiment. 3) A uniform cross-shelf wind stress is applied at zero time over the entire shelf and held constant for the duration of the experiment.

The boundary condition which is most transparent to waves consists of a sponge at the outer edge of the model domain with an Orlanski radiation condition at the outer edge of the sponge. Several open boundary conditions perform adequately in the wind stress experiments, but the Orlanski radiation condition alone (without a sponge) appears to give the best total performance (of those tested) through all of the experiments. It is adequate at transmitting wave energy, and its response is entirely acceptable in the wind stress experiments.

The results suggest that a clamped open boundary is probably the worst choice of cross-shelf open boundary condition for barotropic coastal models. In fact, any open boundary condition which significantly restricts the cross-shelf open boundary should probably be avoided.

1. Introduction

Numerical models of finite coastal ocean regions inevitably involve the treatment of open boundaries (typically two cross-shelf and one offshore) where the numerical grid ends, but where the fluid motion should be unrestricted. Ideal open boundaries are transparent to motions which are generated within the computational domain and which are felt at the open boundaries (i.e., waves, mean flows, etc.). Unfortunately, there is no numerical treatment of open boundaries which achieves this ideal for general models which include two (or three) dimensions, rotation, variable depth, bottom friction and wind stress forcing. Consequently, it has been suggested that approximate, *ad hoc* open boundary conditions (OBCs) may be the most reasonable approach to the problem at this time (Bennett and McIntosh, 1982).

Since any *ad hoc* OBC will introduce inaccuracies into the numerical solution, it is important to evaluate each OBC and to choose the most effective one. Typically, one of two approaches is taken. First, the model may be suitably simplified so that analytical solutions exist, thus allowing a quantitative comparison of numerical results with analytical solutions (e.g., Chen, 1973; Davies, 1983). However, the simplifications often eliminate essential features of the model making it difficult to assess the performance of the same OBC in the original model. A second approach is to run the complicated numerical model several times, using a different OBC each time. The results are then compared in an attempt to understand the differences (e.g., Flagg *et al.*, 1982). However, this approach may not add insight into the general effects of the OBCs when applied to other models, and it may not isolate the physical mechanism(s) by which the different OBCs affect the solution. Further, this may be an expensive approach if the model is large.

The present study is essentially an attempt to combine the desirable features of the two approaches described above. A number of different OBCs are used at the cross-shelf open boundaries of a numerical model of barotropic coastal flow for which analytical solutions are generally unavailable. (The offshore open boundary is held clamped throughout for reasons given later.) The OBCs are chosen based on the simplicity of implementation, their common usage and the possibility of reasonable physical behavior. Only OBCs which are applied on a point-by-point basis are considered, so that no special geometry or physics need be assumed. Because an OBC may perform differently under different physical circumstances, three numerical experiments are performed; (i) barotropic relaxation, (ii) alongshelf wind stress,

* Woods Hole Oceanographic Institution Contribution Number 5828.

and (iii) cross-shelf wind stress. Each experiment is designed to allow some simple analytical analyses to interpret physically the behavior of the model.

An *a priori* assumption is made that the region outside the model domain is initially quiescent and does not influence the flow inside the model domain. While this assumption may not be realistic for *predictive* studies of real ocean currents, it is applicable to *process-oriented* studies of isolated physical phenomena in coastal regions. Furthermore, the difficulties associated with OBCs are usually compounded by the presence of flow outside the model domain. For example, if variables are specified along open boundaries, based on observations, it is difficult to distinguish in the interior between effects introduced by the OBCs and effects introduced by errors in the specified quantities. Therefore, the present approach seems to be a reasonable first attempt at building some insight into the effects that these OBCs might have in more general contexts. Hopefully, this study will also encourage the testing and comparison of other OBCs.

The numerical model used here is a modified version of that developed by Beardsley and Haidvogel (1981; hereinafter BH) and is described briefly in Section 2. The OBCs are defined in Section 3. The results of the numerical experiments appear in Section 4, followed by a summary in Section 5.

2. The numerical model

The numerical model is described in detail by BH. The equations to be solved are the vertically-integrated and linearized momentum and continuity equations for a homogeneous fluid with surface and bottom stresses:

$$u_t - fv = -gh\zeta_x + \frac{\tau_s^x}{\rho} - \frac{\tau_b^x}{\rho} \tag{2.1a}$$

$$v_t + fu = -gh\zeta_y + \frac{\tau_s^y}{\rho} - \frac{\tau_b^y}{\rho} \tag{2.1b}$$

$$u_x + v_y + \zeta_t = 0 \tag{2.1c}$$

where (u, v) are the transports in the alongshelf (x) and cross-shelf (y) directions, f is the Coriolis parameter, g gravitational acceleration, h water depth, ζ sea surface elevation, ρ the fluid density, (τ_s^x, τ_s^y) the (x, y) wind stress components, and (τ_b^x, τ_b^y) and (x, y) bottom stress components. Subscripts (x, y, t) denote partial differentiation. Solutions are obtained by finite differences on a staggered (Arakawa C) grid in a manner identical to BH except that their quadratic bottom stress is here replaced by a linear bottom stress of the form

$$(\tau_b^x, \tau_b^y) = \frac{\rho r}{h}(u, v) \tag{2.1d}$$

where r is a (constant) resistance coefficient with dimensions of velocity. For numerical stability, the terms in (2.1d) are included in a semi-implicit form. The differences resulting from the two forms of the assumed bottom drag are negligible, but the use of (2.1d) keeps the problem linear which facilitates comparisons with simple analytical models.

3. Open boundary conditions

In a coastal ocean model there are typically three open boundaries—one offshore and two cross-shelf. Under most circumstances, the offshore boundary can be argued to be the least significant because the steep continental slope strongly refracts surface gravity waves and virtually prevents cross-shelf geostrophic flow in a barotropic model (e.g., Wang, 1982). In fact, as the deep-ocean depth becomes large, shelf motions become uncoupled from deep-sea motions. Thus, an infinitely deep ocean bordering the shelf may be approximated by a clamped boundary, in which the open boundary variables are fixed at zero throughout the computations. Further, for a very deep (but finite depth) deep ocean, this choice should not affect the numerical results as much as the choice of cross-shelf OBCs. Therefore, all of the numerical experiments described in Section 4 utilize a clamped offshore boundary (located one grid space seaward of the shelf break) so that only the effects of the cross-shelf OBCs are considered.

The cross-shelf open boundaries in the present experiments are always imposed along lines of constant x ($x = 0$, $x = W$). The staggered grid of the present model requires that the sea surface elevation and the velocity tangent to the open boundary must be specified or computed along each open boundary at each time step. Thus, each OBC is applied to both the sea surface elevation (ζ) and the cross-shelf velocity (v).

a. Numerical approximations

Seven different OBCs are considered, most of which are basically Sommerfeld radiation conditions of the form

$$\phi_t \pm c\phi_x = 0 \tag{3.1}$$

with a different prescription for the phase speed (or advection velocity) c. The variable ϕ represents either the sea surface elevation or the cross-shelf velocity. The upper sign in (3.1) is used at the right open boundary ($x = W$) while the lower sign is used at the left open boundary ($x = 0$). Because the interior points have been updated when the OBCs are applied, it is sometimes possible to implement (3.1) in either implicit or explicit form. This has been done with four of the seven OBCs, making a total of eleven OBCs whose analytical and numerical forms are presented in Table 1. Again the upper (lower) sign of $\pm$ or $\mp$ refers to the right (left) open boundary. The OBCs are:

TABLE 1. Analytical and numerical forms of the OBCs, as well as their reflection coefficients for a single wave (with frequency ω and wavenumber k) for the special case discussed in Section 3b. ϕ represents either sea surface elevation or cross-shelf velocity, whichever is to be updated using the OBCs. The upper (lower) sign in $\pm$ and $\mp$ corresponds to the open boundary at the right (left) side of the model. Subscript B represents the boundary grid-point. Other variables are; Δx the grid spacing, Δt the time step, c the phase speed, $\mu = c\Delta t/\Delta x$ (except where noted), T_f a friction time scale, r_m the maximum friction in the sponge, n the number of grid points in the sponge, and r_i the bottom friction in the interior domain.

Open boundary condition	Analytical form	Numerical form	Reflection coefficient (ϕ_R)
1. Clamped (CLP)	$\phi = 0$	$\phi_B^{n+1} = 0$	-1
2. Gradient (GRD)	$\phi_x = 0$	$\phi_B^{n+1} = \phi_{B\mp1}^{n+1}$	$e^{ik\Delta x}$
3. Gravity–wave radiation: Explicit (GWE)	$\phi_t \pm c\phi_x = 0 \quad c = (gh)^{1/2}$	$\phi_B^{n+1} = \phi_B^n - \mu(\phi_B^n - \phi_{B\mp1}^n)$	$-(e^{i\omega\Delta t} - 1 + \mu - \mu e^{ik\Delta x})/(e^{i\omega\Delta t} - 1 + \mu - \mu e^{-ik\Delta x})$
4. Gravity–wave radiation: Implicit (GWI)	Same as GWE	$\phi_B^{n+1} = (\phi_B^n + \mu\phi_{B\mp1}^{n+1})/(1 + \mu)$	$\dfrac{-[e^{i\omega\Delta t} - (1 + \mu e^{i\omega\Delta t + ik\Delta x})/(1 + \mu)]}{[e^{i\omega\Delta t} - (1 + \mu e^{i\omega\Delta t - ik\Delta x})/(1 + \mu)]}$
5. Partially clamped: Explicit (PCE)	$\phi_t \pm c\phi_x = -\phi/T_f \quad c = (gh)^{1/2}$	$\phi_B^{n+1} = \phi_B^n\left(1 - \dfrac{\Delta t}{T_f}\right) - \mu(\phi_B^n - \phi_{B\mp1}^n)$	$\dfrac{-\left[e^{i\omega\Delta t} - 1 + \mu + \dfrac{\Delta t}{T_f} - \mu e^{ik\Delta x}\right]}{\left[e^{i\omega\Delta t} - 1 + \mu + \dfrac{\Delta t}{T_f} - \mu e^{-ik\Delta x}\right]}$
6. Partially clamped: Implicit (PCI)	Same as PCE	$\phi_B^{n+1} = \left[\phi_B^n\left(1 - \dfrac{\Delta t}{T_f}\right) + \mu\phi_{B\mp1}^{n+1}\right]\Big/(1 + \mu)$	$\dfrac{-\left[e^{i\omega\Delta t} - \left(1 - \dfrac{\Delta t}{T_f} + \mu e^{i\omega\Delta t + ik\Delta x}\right)\Big/(1 + \mu)\right]}{\left[e^{i\omega\Delta t} - \left(1 - \dfrac{\Delta t}{T_f} + \mu e^{i\omega\Delta t - ik\Delta x}\right)\Big/(1 + \mu)\right]}$
7. Orlanski radiation: Explicit (ORE)	$\phi_t \pm c\phi_x = 0$	$\phi_B^{n+1} = [\phi_B^{n-1}(1 - \mu) + 2\mu\phi_{B\mp1}^n]/(1 + \mu)$	0

$$c = \begin{cases} \dfrac{\Delta x}{\Delta t} & \text{if} \quad \mp\phi_t/\phi_x \geq \dfrac{\Delta x}{\Delta t} \\ \mp\phi_t/\phi_x & \text{if} \quad 0 < \mp\phi_t/\phi_x < \dfrac{\Delta x}{\Delta t} \\ 0 & \text{if} \quad \mp\phi_t/\phi_x \leq 0 \end{cases}$$

$$\mu = \begin{cases} 1 & \text{if} \quad C_L \geq 1 \\ C_L & \text{if} \quad 0 < C_L < 1 \quad C_L = \dfrac{\phi_{B\mp1}^{n-2} - \phi_{B\mp1}^n}{\phi_{B\mp1}^n + \phi_{B\mp1}^{n-2} - 2\phi_{B\mp2}^{n-1}} \\ 0 & \text{if} \quad C_L \leq 0 \end{cases}$$

8. Orlanski radiation: Implicit (ORI)	Same as ORE	Same as ORE except $C_L = \dfrac{\phi_{B+1}^{n-1} - \phi_{B+1}^{n+1}}{\phi_{B+1}^{n+1} - \phi_{B+1}^{n-1} - 2\phi_{B+2}^{n}}$	0
9. Modified Orlanski radiation: Explicit (MOE)	$\phi_t \pm c\phi_x = 0$ $c = \begin{cases} \Delta x/\Delta t & \text{if } \mp\phi_t/\phi_x > 0 \\ 0 & \text{if } \mp\phi_t/\phi_x \leqslant 0 \end{cases}$	$\phi_B^{n+1} = \begin{cases} \phi_{B+1}^{n} & \text{if } C_L > 0 \\ \phi_B^{n-1} & \text{if } C_L \leqslant 0 \end{cases}$ C_L is same as in ORE	$-(e^{i\omega\Delta t} - e^{ik\Delta x})/(e^{i\omega\Delta t} - e^{-ik\Delta x})$
10. Modified Orlanski radiation: Implicit (MOI)	Same as MOE	Same as MOE except C_L is evaluated as in ORI	Same as MOE
11. Sponge plus Orlanski radiation (SPO)	a. Sponge outside open boundary: $r = \alpha(x_B \pm x) + r_i$ where r_i = interior r, α = const., x_B = boundary location b. ORI is applied at the outer edge of sponge	a. $r = \dfrac{r_m - r_i}{n}(B - j) + r_i \quad j = B \pm 1, 2, \cdots n$ n = grid points in sponge; r_m = maximum r at outer edge of sponge b. Same as ORI	

i) *Clamped* (CLP): This condition (used by BH) assumes $c = 0$ in (3.1) and is the most restrictive OBC in the sense that the boundary values do not evolve in time with the interior solution. Geostrophic flow normal to the open boundary is eliminated although both surface and bottom Ekman transport across the open boundary are allowed.

ii) *Gradient* (GRD): This condition assumes $c = \infty$ in (3.1). The boundary values evolve in time, and geostrophic flow normal to the boundary is allowed.

iii) *Gravity–Wave Radiation:* This condition may be implemented in either implicit (GWI) or explicit (GWE) form. The phase speed in (3.1) is chosen to be the local, flat-bottom, shallow-water surface gravity wave speed, $c = (gh)^{1/2}$.

iv) *Partially Clamped:* This condition is identical to the gravity-wave radiation condition, but it includes an *ad hoc* "friction-like" term $(-\phi/T_f)$ on the right hand side of (3.1), where T_f is a friction time scale. It may be implemented in either implicit (PCI) or explicit (PCE) form. PCE was introduced by Blumberg and Kantha (1982) as a means of slowing the emptying of their basin which occurred using GWE.

v) *Orlanski Radiation:* The phase speed at which ϕ is approaching the boundary is evaluated at each time step from values of ϕ near the boundary. This computed phase speed is then used in (3.1) at the boundary. Orlanski (1976) used an explicit form (ORE) for the phase speed, but an implicit form (ORI) is also possible.

vi) *Modified Orlanski Radiation:* This condition (suggested by Camerlengo and O'Brien, 1980) uses only the extreme values of phase speed from the Orlanski Radiation boundary condition ($c = 0$ or $\Delta x/\Delta t$) computed in explicit (MOE) or implicit (MOI) form.

vii) *Sponge Plus Orlanski Radiation* (SPO): This condition combines a sponge with an absorbing boundary as suggested by Israeli and Orszag (1981). In the present experiments, the sponge is a region of increasing bottom friction and the absorbing boundary is the ORI condition imposed at the outer edge of the sponge.

b. Boundary reflection for a special case

Before proceeding with the numerical experiments, it is instructive to consider the behavior of the OBCs under fairly simple conditions. At steady state (3.1) becomes $\phi_x = 0$, so all OBCs of the form (3.1) should produce identical steady state solutions independent of c. This includes all of the present OBCs (Table 1) except CLP, PCE, PCI and SPO whose steady state solutions may differ from the others. On the other hand, the approach to steady state depends primarily on the transient response of the system and the way in which an OBC handles that response.

Barotropic coastal models adjust by radiating surface gravity waves, edge waves and shelf waves which ideally would be transmitted through the open boundaries with no wave reflection. To develop an initial understanding of the transient behavior of the OBCs considered here, their wave reflection properties can be evaluated analytically for the special case of a one-dimensional, flat-bottom basin. Consider a wave of unit amplitude traveling in the $+x$ direction with frequency ω and wavenumber k. Upon encountering an OBC at $x = 0$, a reflected wave may be generated which travels in the $-x$ direction with complex amplitude ϕ_R (relative to the incident wave amplitude). The sum of the incident and reflected waves,

$$\phi_j^n = e^{i(\omega n\Delta t - kj\Delta x)} + \phi_R e^{i(\omega n\Delta t + kj\Delta x)} \qquad (3.2)$$

where $t = n\Delta t$, $x = j\Delta x$, must satisfy the numerical form of each OBC. Substitution of (3.2) into the OBCs results in the reflection coefficients (ϕ_R) listed in Table 1. (This procedure does not work for SPO due the presence of the sponge layer.)

Some of the reflection coefficients are easy to evaluate. The CLP and GRD conditions are perfect reflectors in that the amplitude of the reflected wave $|\phi_R|$ is unity, independent of ω and k. The clamped condition produces a phase shift of π while GRD results in a phase shift of $k\Delta x$. At the other extreme, the ORE and ORI conditions are perfect absorbers, producing no reflected wave.

All of the other OBCs become perfectly transmitting boundaries as $k\Delta x$, $\omega\Delta t \to 0$. However, in general, their reflection properties depend on the incident frequency and wavenumber as well as the numerical grid space, time step and phase speed. Figure 1 shows contours of $|\phi_R|$ on the ($\omega\Delta t$, $k\Delta x$) plane for several OBCs. The GWE (Fig. 1a) and GWI (Fig. 1b) conditions have minima along the line $\omega\Delta t = \mu k\Delta x$ ($\mu = c\Delta t/\Delta x = 0.5$ in Figs. 1a, b) which is equivalent to $\omega = ck$; i.e., the phase speed of the incident wave is identical to the assumed phase speed for the OBC. The reflection amplitude increases in all directions away from that line. There is always some reflection along this minimum due to numerical dispersion (except when $\mu = 1$ so that the grid points lie on the wave characteristic). There is greater reflection from GWI than GWE for any choice of ($\omega\Delta t$, $k\Delta x$). Figure 1c represents the reflection due to MOE and MOI which is independent of c because only a single phase speed is used. It is also identical to the reflected wave amplitude using GWE when $\mu = 1$. The reflection coefficients for PCE and PCI are different from those of GWE and GWI, respectively, only in the factor $\Delta t/T_f$ in both numerator and denominator (see Table 1). For a typical time step of $\Delta t = 150$ sec. and the friction-time recommended by Blumberg and Kantha (1982) of $T_f = 4$ hours, then $\Delta t/T_f \approx 0.01$ and the reflection coefficient differences between PCE and GWE and between PCI and GWI are negligible. Not

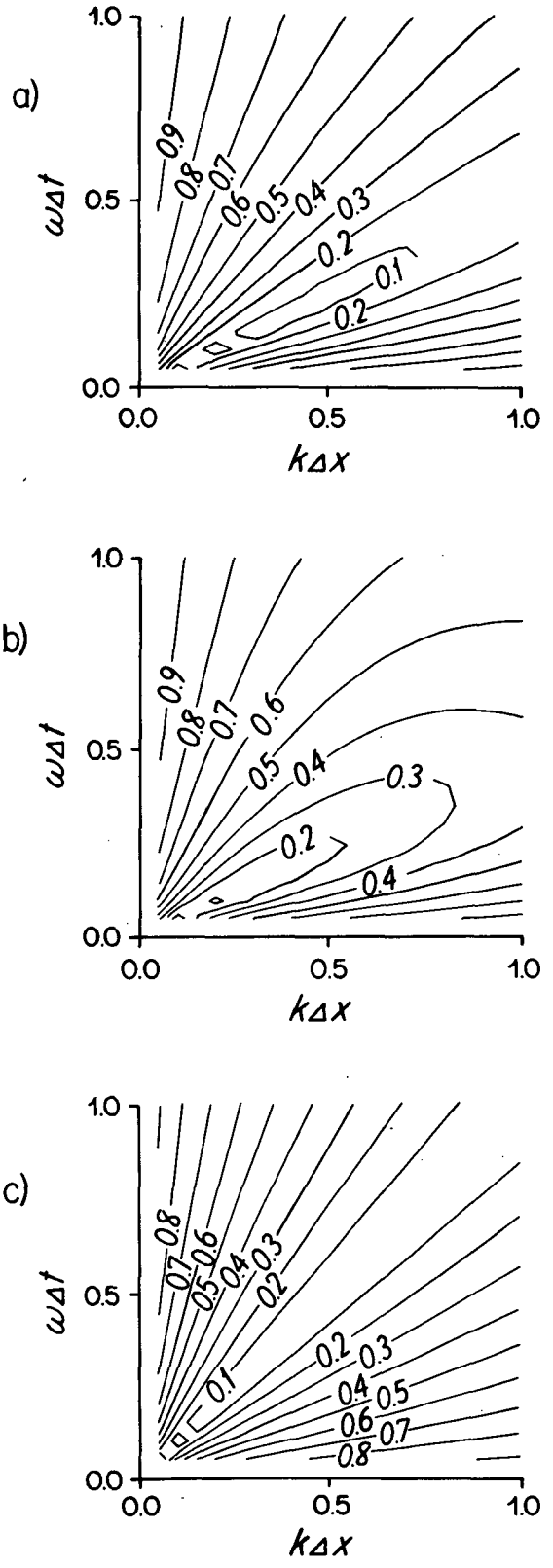

FIG. 1. Amplitude of the reflection coefficient $|\phi_R|$ from Table 1 for (a) GWE with $\mu = 0.5$, (b) GWI with $\mu = 0.5$, (c) MOI, MOE or GWE with $\mu = 1$.

surprisingly, these results all show that the amplitude of the reflected wave is directly proportional to the mismatch between ω/k and the assumed phase speed c.

Once a reflected wave has been generated, it remains in the interior domain either until bottom friction damps it out or until it encounters another open boundary where some of the wave may be transmitted through the boundary and some may be reflected. The effectiveness of bottom friction in damping the reflected waves can be estimated for a monochromatic wave with frequency ω and wavenumber k in a nonrotating, one-dimensional (x) channel of uniform depth h. Equations (2.1) simplify to

$$\zeta_{xx} + \frac{\omega^2}{gh}\left(1 - \frac{ir}{\omega h}\right)\zeta = 0 \tag{3.3a}$$

with the corresponding dispersion relation

$$k^2 = \frac{\omega^2}{gh}\left(1 - \frac{ir}{\omega h}\right). \tag{3.3b}$$

For typical midshelf values of $r = 0.05$ cm s^{-1}, $h = 50$ m and $\omega = 0.001$ s^{-1}, then $r/\omega h = 0.01 \ll 1$. From (3.3b) the decay time scale (choosing k real) is approximately $T_r \approx 2h/r = 55.5$ hours while the decay length scale (choosing ω real) is approximately $L_r \approx 2h(gh)^{1/2}/r = 4.4 \times 10^3$ km. Thus, bottom friction alone is not very effective for wave dissipation in space or time and should not be relied upon to remove undesired reflected wave energy.

These simple examples help to illustrate some similarities as well as some differences between the various OBCs. While the results of this section cannot be simply extended to include two dimensions, variable depth, multiple waves, etc., they do suggest that the transient behavior of a model may be strongly affected by the choice of OBCs. In the next section, the proposed OBCs will be used in several experiments in order to compare their effects in more general situations.

4. Numerical experiments

To examine the effects of the OBCs in the barotropic coastal model described by (2.1), three numerical experiments have been conducted with each OBC. The experiments are simple enough to allow some analytical analysis of the results while still retaining the important dynamical features of variable depth, rotation and bottom friction. The topography and boundaries for each experiment are shown in Fig. 2. Boundaries are coastal at $y = 0$, offshore at $y = -L$ and cross-shelf at $x = 0$, W. The OBCs are applied at $x = 0$, W. The grid spacing is $\Delta x = \Delta y = 10$ km, which is fine enough to handle resolvable edge waves quite accurately (see the Appendix). A fairly small grid of 17 alongshelf points and 12 cross-shelf points is used (i.e., $L = 105$ km, $W = 160$ km) which serves

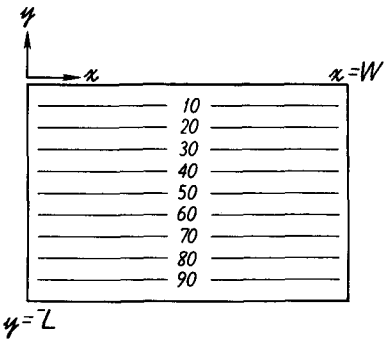

FIG. 2. Topography and boundaries for the present experiments. The coast is at $y = 0$, the deep ocean at $y = -L$ and open cross-shelf boundaries at $x = 0$, W. Depths are in meters.

to accentuate the effects of the OBCs. The topography varies only in the cross-shelf direction. The depth at the coast is 3 m because of the staggered grid, while the depth at $y = -L$ is 2000 m. The maximum shelf depth is 95 m which occurs one grid space shoreward of the offshore boundary. Thus, the bottom slope over most of the shelf is $h_y = -0.001$. The complete topography is given by

$$h = \begin{cases} 300 - 0.0004y, & -5 \times 10^5 < y < 0 \\ -0.001y, & -95 \times 10^5 < y < -5 \times 10^5 \\ -1.80025 \times 10^6 - 0.1905y, & y < -95 \times 10^5 \end{cases} \tag{4.1}$$

where h and y are in cm. For most of the analytical analysis, the bottom slope will be assumed constant ($h_y = -0.001$) with little imposed error. When the error is appreciable, (4.1) must be used. (Note that the offshore boundary is always clamped, so that the deep-ocean depth only enters the calculations when averaged with neighboring depths.) The bottom friction coefficient is fixed at either $r = 0$ or $r = 0.05$ cm s^{-1}. The Coriolis parameter is taken as $f = 10^{-4}$ s^{-1} and the density is assumed to be $\rho = 1$ gm cm^{-3}. The time step is $\Delta t = 150$ sec. Additional details of the finite-difference scheme may be found in BH.

a. *Barotropic relaxation*

This experiment is designed to investigate the wave reflection properties of the various OBCs in more general circumstances than considered in Section 3b. Following BH, the fluid is initially at rest with the sea surface elevated in a symmetrical mound centered at the middle of the computational domain with elevation maximum at the coast and linearly decreasing offshore;

$$\zeta_{jm}(t = 0) = \begin{cases} (m - 4)\sin^2[\pi(j - j_m + 5)/10] & \text{if} \\ \quad -4 < j - j_m < 4, \quad 5 < m < 11 \\ 0, \quad \text{otherwise} \end{cases} \tag{4.2}$$

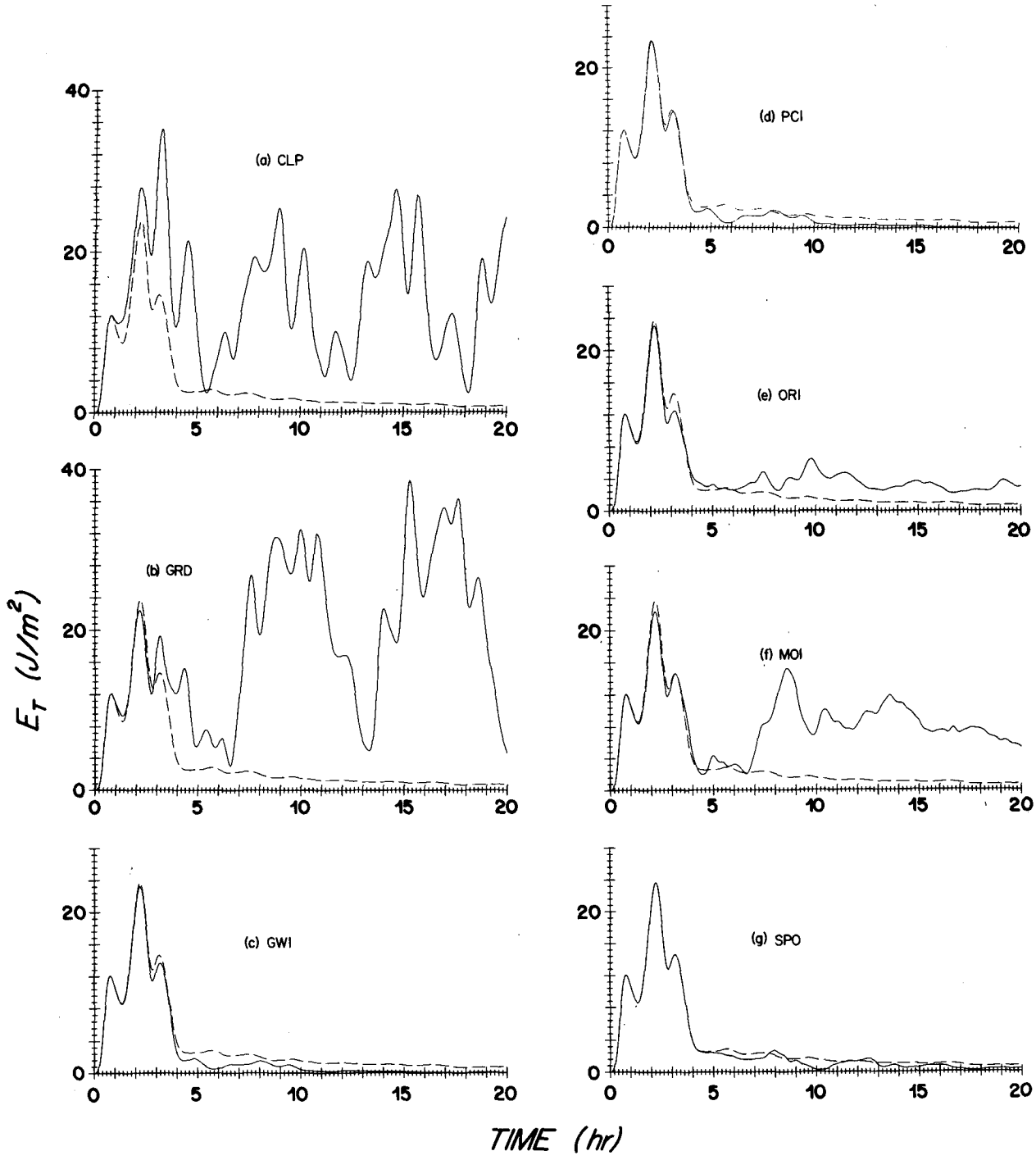

FIG. 3. Total energy (E_T), along a cross-shelf transect at $j = j_m + 5$ given by (4.3), versus time for the first 20 h of the barotropic relaxation experiment. The dashed curve is the result for the large domain which represents perfectly transparent cross-shelf boundaries in the small domain. The solid curve is E_T when using (a) CLP, (b) GRD, (c) GWI, (d) PCI, (e) ORI, (f) MOI, (g) SPO.

where j_m is the grid point in the middle of the numerical domain and $y = m\Delta y$. As the fluid relaxes, surface gravity waves, edge waves and continental shelf waves radiate from the center mound and impinge on the open boundaries at $x = 0(j = 1)$ and $x = W(j = 17)$. To simulate the model response with perfectly transparent open boundaries, the same experiment was performed on a large grid with 101 alongshelf grid points and the mound centered at $j_m = 51$. The calculations were halted before any reflec-

tions from the boundaries of the large grid had affected the middle 17 grid points.

As a diagnostic, the total energy (kinetic plus potential) along the cross-shelf transect at $j_m + 5$ was computed at each time step;

$$E_T = \frac{1}{2} \sum_{\substack{m=2 \\ j=j_m+5}}^{11} \left\{ \frac{1}{h_{jm}} \left[\left(\frac{u_{jm} + u_{j+1m}}{2} \right)^2 + \left(\frac{v_{jm} + v_{jm+1}}{2} \right)^2 \right] + g\zeta_{jm}^2 \right\}. \quad (4.3)$$

(The choice of diagnostic is arbitrary. The present choice allows reflections to be seen clearly whereas other choices, for example the total energy in the domain, may not.) Several plots of E_T versus time for selected OBCs are shown in Fig. 3 for the first 20 hours of each run with no bottom friction ($r = 0$). The results for the large domain (dashed; meant to represent the small domain with perfect OBCs) and for the small domain with the OBCs imposed (solid) are shown. For this experiment, SPO was used with no interior friction ($r_i = 0$), maximum sponge friction of $r_m = 0.1$ and a sponge four grid spaces in width ($n = 4$; a fairly thin sponge). For each run, the rms error [the standard deviation of the difference between the large domain and small domain energies from (4.3)] is listed in Table 2.

The high reflectivity of CLP and GRD is obvious in Figs. 3a, b and from the large standard deviations in Table 2. (Note that, although energy is conserved in the small domain with both CLP and GRD, the amplitude of the response at $j = j_m + 5$ increases due to multiple reflections which set up standing wave components.) Conditions GWE (not shown) and GWI (Fig. 3c) show a marked improvement over CLP and GRD, although they consistently underpredict the energy at large times. At short times, the fast gravity waves are reaching the boundaries with phase speeds close to $(gh)^{1/2}$. At larger times, the slower edge waves are reaching the boundaries with phase speeds less than $(gh)^{1/2}$. So, GWE and GWI overestimate the edge wave phase speeds and consequently remove energy and mass too rapidly. This is presumably the cause of the basin-emptying in Blumberg and Kantha's (1982) work. Note that in Section 3b, GWI showed higher reflectivity than GWE. In the present experiment this higher reflectivity partially counterbalances the rapid loss of energy and mass, leading to an apparently less reflective result for GWI. The PCE and PCI conditions reduce this basin-emptying effect by further increasing the reflective nature of the boundaries (compare Fig. 3c and 3d at times between 5 and 10 hours). The ORE and ORI conditions, although being perfect absorbers in one-dimension, show some reflection here with ORI (Fig. 3e) being a considerable improvement over ORE (Table 2). The MOE (not shown) and MOI (Fig. 3f) conditions show substantial reflection, neither being an improvement over ORI. The best results are clearly obtained by using SPO with a fairly small maximum bottom friction $r_m \approx 0.1$ (Fig. 3g and Table 2). The condition

TABLE 2. Selected results from the numerical experiments. First column identifies the OBCs. Second column is the rms error due to each OBC in the barotropic relaxation experiment with no bottom friction ($r = 0$). Third column is the same as the second column with $r = 0.05$. Fourth column is the maximum bottom friction r_m of the sponge layer used with SPO. Fifth column is the alongshelf velocity near the coast in the alongshelf wind stress experiment after 72 h. Sixth column is the sea surface elevation near the coast in the cross-shelf wind stress experiment after 72 h.

Open boundary condition	Barotropic relaxation rms error (J/m^2)			Alongshelf wind stress u/h at (j, m) = (9, 11) after 72 h ($cm\ s^{-1}$)	Cross-shelf wind stress ζ at (j, m) = (9, 11) after 72 h (cm)
	$r = 0$	$r = 0.05$	r_m		
CLP	1.302	0.471		−17.24	1.52
GRD	1.925	0.753		−20.00*	2.96*
GWE	0.104				
GWI	0.096	0.073		−19.82	2.77
PCE	0.078				
PCI	0.078	0.058		−18.10	1.74
ORE	0.620				
ORI	0.200	0.147		−19.88	2.85
MOE	0.510				
MOI	0.634	0.316		−19.92	2.86
SPO	0.094		0.0		
SPO	0.049		0.05		
SPO	0.047		0.10		
SPO	0.052		0.25		
SPO	0.051		0.5		
SPO	0.059		1.0		
SPO	0.081		2.0		
SPO		0.034	0.15	−18.04	2.89
analytical				−20.00	3.02

* Still oscillating

SPO is very accurate at small times partly due to the sponge layer and partly due to the increased size of the computational domain (i.e., waves take longer to reflect from the ORI boundary and return to the small grid). In fact, there has been little attempt at optimizing SPO which could be further improved by adjusting the size of the sponge layer n and the maximum bottom friction r_m or constructing an entirely different sponge. However, this is beyond the scope of this paper and the reader is referred to Israeli and Orszag (1981) for a more complete discussion of the effects of sponge-layer size and friction.

Snapshots of sea surface elevation ζ in the small domain after 4 hours support the above results. The CLP (Fig. 4a), GRD (Fig. 4b), and MOI (Fig. 4f) results show little resemblance to the large domain (uppermost panel). The GWI (Fig. 4c) and PCI (Fig. 4d) results are nearly identical with each other and contain features similar to the large domain, but they are contaminated by small-scale features (short waves).

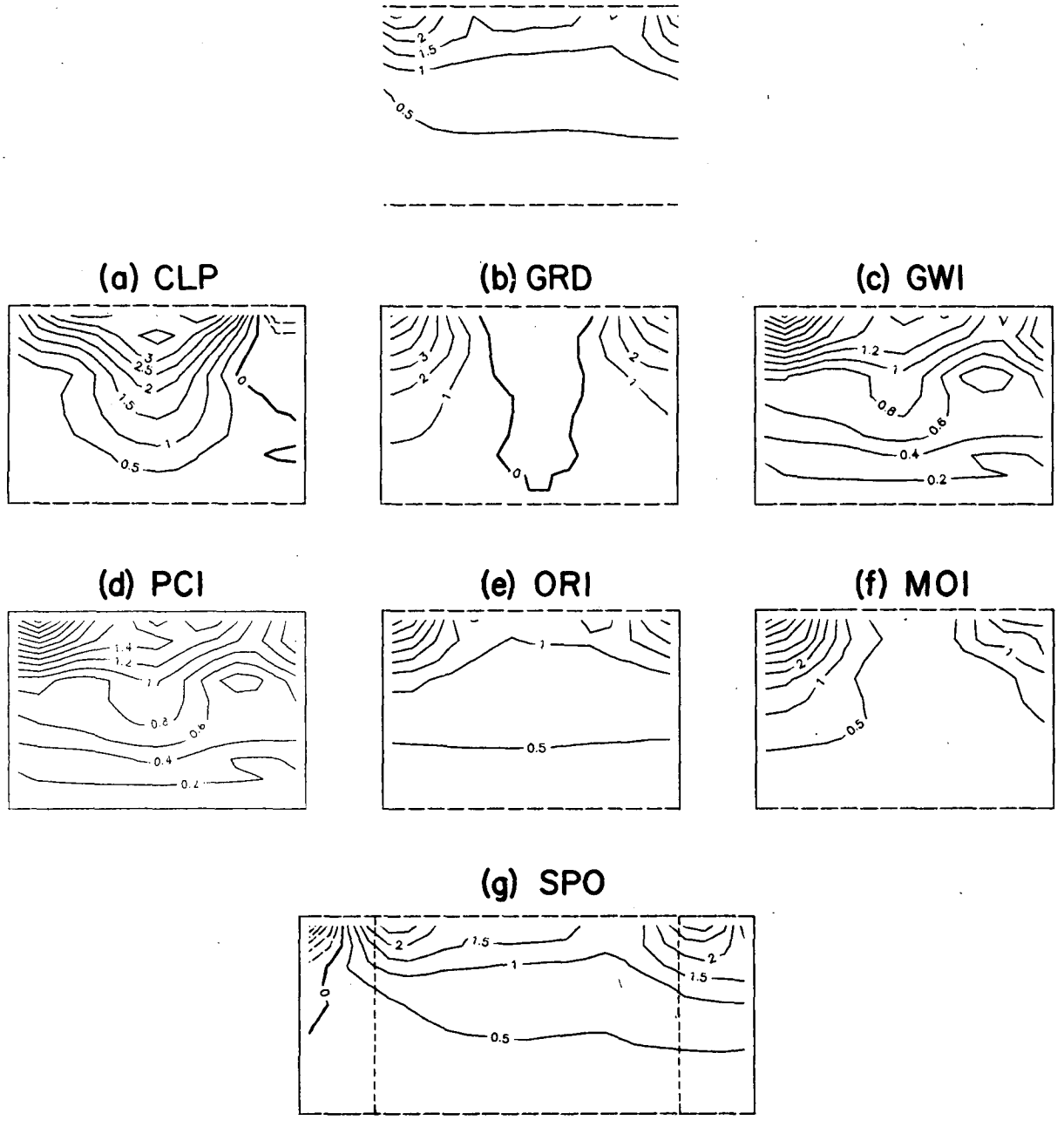

FIG. 4. Snapshots of sea-surface elevation contours (cm) after 4 h in the barotropic relaxation experiment. The upper panel is the middle section of the large domain (no reflection at $x = 0$, W). Other panels correspond to (a) CLP, (b) GRD, (c) GWI, (d) PCI, (e) ORI, (f) MOI, (g) SPO (dashed lines indicate the beginning of sponge region).

This occurs because edge-wave phase speeds are not depth dependent, whereas GWE, GWI, PCE and PCI all assume depth dependent phase speeds. Therefore the edge waves are necessarily distorted and scatter into smaller-scale waves. The ORI (Fig. 4e) result is quite similar to the large domain, while the SPO (Fig. 4g) result is almost identical to the large domain.

The addition of bottom friction in the computational domain ($r = 0.05$ cm s^{-1}) reduces the standard deviations in Table 2. It does not, however, alter the general conclusion that SPO is more transparent to waves than any of the other OBCs considered here. GWE, GWI, PCE, PCI and ORI appear to be reasonably transparent, while CLP, GRD, ORE, MOE, MOI are unacceptably reflective and should be avoided in this type of experiment.

b. *Alongshelf wind stress*

Of major importance when modelling coastal circulation is the response of the water to an applied surface wind stress. To examine the effect of each OBC on the wind-driven response, an impulsive alongshelf wind stress of $\tau_s^x = -1$ dyn cm^{-2} is applied over the entire computational domain at time $t = 0$ and continued for 72 hours.

Although an analytical solution to (2.1) for this problem is unavailable, some insight can be gained from a somewhat simplified analysis of the transient response of an infinitely long coast (which the OBCs are supposed to mimic). If the alongshelf sea-surface slope and the cross-shelf transport are very small ($\zeta_x \ll 1$, $v \ll 1$) then (2.1a) simplifies to

$$u_t = \frac{\tau_s^x}{\rho} - \frac{ru}{h} \tag{4.4}$$

from which

$$u = \frac{h\tau_s^x}{\rho r}(1 - e^{-tr/h}). \tag{4.5}$$

This suggests an adjustment time of h/r for u to reach steady state. Thus, the alongshelf transport in shallow depths should reach steady state faster than in large depths. With $r = 0.05$ cm s^{-1}, then u at 5 m depth takes 2.8 hours to reach steady state, while u at 100 m depth takes 56 hours to reach steady state.

With the same assumptions the alongshelf flow in (2.1b) is in geostrophic balance, $fu = -gh\zeta_y$, so from (2.1a, b)

$$\zeta(y) = \frac{-f\tau_s^x}{\rho g r}\int_{-L}^{y}(1 - e^{-tr/h})dy. \tag{4.6}$$

The adjustment of sea surface elevation at offshore distance y depends on all of the time scales h/r between the offshore boundary and y. Thus, the ζ adjustment time scale will be determined by the largest h/r between the offshore boundary and y and may be quite different from the u adjustment time scale. Physically this means that the steady-state sea surface tilt (ζ_y) sets up rapidly in shallow water generating an alongshelf geostrophic current. However, the sea surface continues to rise (while maintaining the same tilt) until the entire shelf is "filled" by the Ekman transport. This sea level rise may last much longer than the u adjustment time near the coast.

A detailed comparison of the numerical results with (4.5) and (4.6) is somewhat unfair because of the assumptions and simplifications involved in obtaining (4.5) and (4.6). (During the adjustment time period, the numerical results are typically within 10 percent of the simple analytical solutions.) However, the different adjustment time scales for ζ and u are apparent in the numerical results. Figure 5a shows hourly averaged velocity (u/h) over the 72 hour experiment at (x, y) = (80 km, −5 km) and (x, y) = (80 km, −45 km) for selected OBCs, while Fig. 5b shows hourly averaged sea surface elevation over the 72 hour experiment at (x, y) = (80 km, −5 km). (The hourly averaging filters out the kind of high-

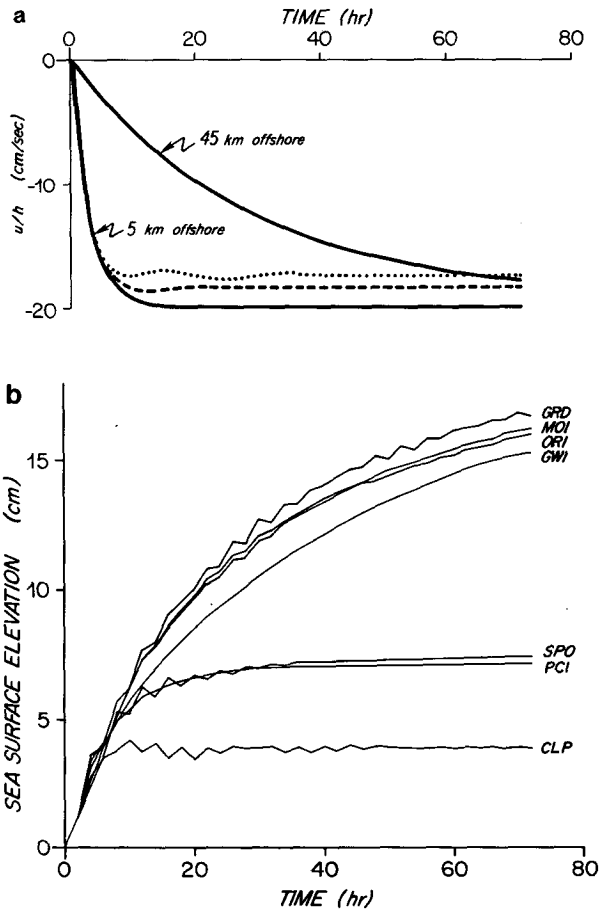

FIG. 5. Time history of (a) alongshelf velocity at (x, y) = (80 km, −5 km) and (x, y) = (80 km, −45 km), and (b) sea surface elevation at (x, y) = (80 km, −5 km) for various OBCs in the alongshelf wind-stress experiment ($\tau_s^x = -1$ dyn cm^{-2}, $r = 0.05$ cm s^{-1}, $f = 10^{-4}$ s^{-1}). In (a), solid curves are results for GRD, GWI, ORI, MOI; dashed curve is for PCI and SPO; dotted curve is for CLP.

frequency transient response which was discussed in Section 4a). The velocity reaches steady state rapidly near the coast and more slowly offshore (as discussed above) regardless of the OBC. According to (4.5) the steady state velocity should be $u/h = \tau_s^x/\rho r = -20$ cm s^{-1} everywhere. The steady values achieved by the various OBCs are listed in Table 2. (Only implicit versions of the OBCs are used here.) The GRD, GWI, ORI and MOI conditions produce virtually identical adjustment in velocity (Fig. 5a; solid curves) and reach almost the same steady state. The CLP, PCI and SPO results, although rapidly reaching a steady state, are not asymptotic to the correct value (Fig. 5a; dashed curve is PCI and SPO, dotted curve is CLP). This difference in behavior is also seen in sea surface elevation (Fig. 5b), where from Eq. (4.6), the steady sea surface elevation at $y = -5$ km should be $\zeta = -(f\tau_s^x/\rho gr)(y + L) = 20.4$ cm. The GRD, GWI, ORI and MOI results show a slow evolution of ζ toward this value, but they have not reached the steady state after 72 hours. The CLP, PCI and SPO conditions produce incorrect steady state values after only a short time.

The reason for the inaccurate behavior using CLP, PCI and SPO is that each of them limits the amount of geostrophic flow which can pass through the open boundary; CLP and PCI through clamping and SPO through increased bottom friction in the sponge. Along an infinite coastline, the alongshelf transport across $x = W$ is equal to the net onshelf Ekman transport per unit alongshelf distance along the coast at $x > W$. The CLP, PCI and SPO conditions do not allow all of this transport to pass through the open boundary and, therefore, do a poor job of representing a section of an infinite coastline. This is even clearer in Fig. 6 where contours of ζ are plotted after 72 hours. Figure 6a is the result for ORI, but GRD, GWI and MOI are similar. The reduced inflow at $x = W$ with CLP (Fig. 6b), PCI (Fig. 6c) and SPO (Fig. 6d) is evidenced by the small cross-shelf gradient in sea surface elevation (ζ_y) near the open boundary.

The effect of the limitation on geostrophic inflow at $x = W$ decreases with distance away from the open boundary because the reduced geostrophic inflow can be compensated by the Ekman transport onto the shelf. To estimate the length of coastline necessary to neglect the effect of the reduced geostrophic inflow, consider the steady version of (2.1) in which the alongshelf flow is assumed geostrophic (as in Csanady, 1978):

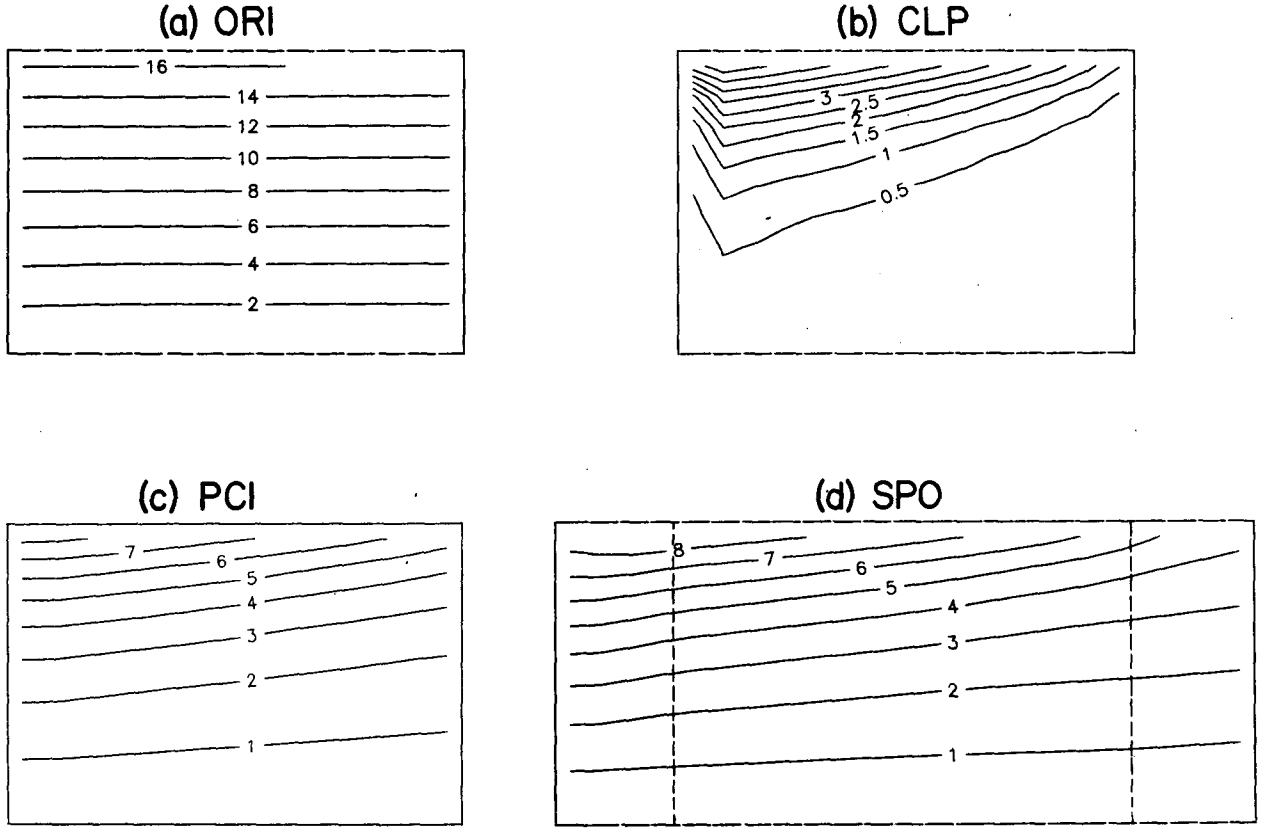

FIG. 6. Contours of sea surface elevation (cm) after 72 hours in the alongshelf wind-stress experiment using (a) ORI, (b) CLP, (c) PCI, (d) SPO ($\tau_s^x = -1$ dyn cm^{-2}, $r = 0.05$ cm s^{-1}, $f = 10^{-4}$ s^{-1}).

$$-fv = -gh\zeta_x + \frac{\tau_s^x}{\rho} - \frac{ru}{h}$$

$$fu = -gh\zeta_y$$

$$u_x + v_y = 0. \tag{4.7}$$

The velocities can be eliminated from (4.7) to obtain

$$\zeta_x + \frac{r}{fh_y}\zeta_{yy} = 0 \tag{4.8a}$$

where h_y is assumed constant. The boundary condition at the coast ($v = 0$ at $y = 0$) becomes

$$\zeta_x - \frac{r}{fh_0}\zeta_y = \frac{\tau_s^x}{\rho g h_0} \quad \text{at} \quad y = 0 \tag{4.8b}$$

where h_0 is the depth at $y = 0$. The offshore boundary is clamped;

$$\zeta = 0 \quad \text{at} \quad y = -L. \tag{4.8c}$$

A solution to (4.8) can be written as

$$\zeta = \frac{-f\tau_s^x}{\rho g r}(y + L) + \sum_{n=0}^{\infty} B_n e^{l_n x} \sin[k_n(y + L)] \tag{4.9}$$

where $k_n \tan(k_n L) = h_y/h_0$, $l_n = k_n^2 r/h_y f$, and the B_n are unknown constants.

For an infinitely long coast, there would be no alongshelf structure, so all the B_n would vanish leaving the steady version of (4.6). Nonzero B_n exist only when the OBC limits the steady flow through the open boundary. Thus, the effect of the limiting OBC decays away exponentially and can be neglected at a distance l_0^{-1} from the open boundary (l_0 is assumed to be the smallest l_n). In the present experiments ($h_y \approx -0.001$, $h_0 = 3$ m, $f = 10^{-4}$ s^{-1}, $r = 0.05$ cm s^{-1}, $L = 105$ km), $k_0 \approx 1.45 \times 10^{-7}$ cm^{-1} and $l_0^{-1} \approx 950$ km. So, the effect of the CLP, PCI and SPO conditions may be felt for roughly 1000 km away from the open boundary. This is a rather serious limitation which makes CLP, PCI and SPO undesirable for problems involving alongshelf wind-driving over long time scales.

The solutions using the other OBCs all behave in a proper physical manner, but they do show some differences which are consistent with the relaxation results of Section 4a. Due to its highly reflective nature, GRD produces a sea surface elevation which oscillates more than using any other OBC, and it still oscillates substantially after 72 hours. The GWI condition consistently predicts smaller sea surface elevations than the others because some mass is being artificially transported out through the open boundaries. The ORI and MOI conditions appear to have the best overall behavior in this experiment.

c. *Cross-shelf wind stress*

The third numerical experiment is another examination of the wind-driven response. An impulsive cross-shelf wind stress of $\tau_s^y = 1$ dyn cm^{-2} is applied over the entire computational domain at $t = 0$ and continued for 72 hours. Along an infinitely long coast, the response consists of oscillations due to gravity waves which radiate away from the coast leaving a steady state setup of sea surface elevation at the coast. There are no alongshelf gradients because identical conditions exist at all x. In the limited domain of the numerical experiment, however, two changes to this scenario occur. First, the cross-shelf OBCs introduce alongshelf gradients, thus changing the adjustment process and possibly the steady state. Second, the offshore clamped boundary (deep ocean of nearly infinite depth) reflects the radiating gravity waves resulting in seiching motions at the natural frequencies of the small domain.

Figure 7 shows the sea surface elevation response at $(x, y) = (70, -5)$ km for several OBCs. In all cases, there are large oscillations initially. These oscillations persist with CLP and GRD, but they rapidly die out with the other OBCs. This is because CLP and GRD are perfect reflectors and keep all of the wave energy inside the domain, thus allowing seiches to be maintained with bottom friction alone causing their decay with time. The other OBCs create alongshelf gradients near the boundaries and radiate energy out of the domain.

To examine the CLP response, consider the nonrotating ($f = 0$), unforced ($\tau_s^x, \tau_s^y = 0$) and frictionless ($r = 0$) version of (2.1) in which all motions occur at frequency ω. Then (2.1) may be combined to eliminate the velocities, yielding

$$\zeta_{xx} + \zeta_{yy} + \frac{h_y}{h}\zeta_y + \frac{\omega^2}{gh}\zeta = 0. \tag{4.10}$$

The x dependence must be $\sin(n\pi x/W)$ where n is any nonzero integer. Thus, (4.10) becomes

$$\zeta_{yy} + \frac{h_y}{h}\zeta_y + \left[\frac{\omega_n^2}{gh} - \left(\frac{n\pi}{W}\right)^2\right]\zeta = 0 \tag{4.11a}$$

with boundary conditions

$$\zeta = 0 \quad \text{at} \quad y = -L$$

$$\zeta_y = 0 \quad \text{at} \quad y = 0. \tag{4.11b}$$

Equation (4.11) has been solved numerically using a shooting technique to find the frequencies ω_n. For increased accuracy, the topography given by (4.1) is used here. The first mode seich frequency $\omega_1 = 4.61 \times 10^{-4}$ s^{-1} which corresponds to a period of 3.79 hours. The observed period in Fig. 7a is 3.64 hours suggesting that the oscillations in Fig. 7a are due to the lowest mode seich (with the CLP conditions).

The GRD response may be examined with rotation included because no alongshelf gradients should be present ($\zeta_x = 0$ at $x = 0, W$). In this case, (2.1) without forcing or friction becomes

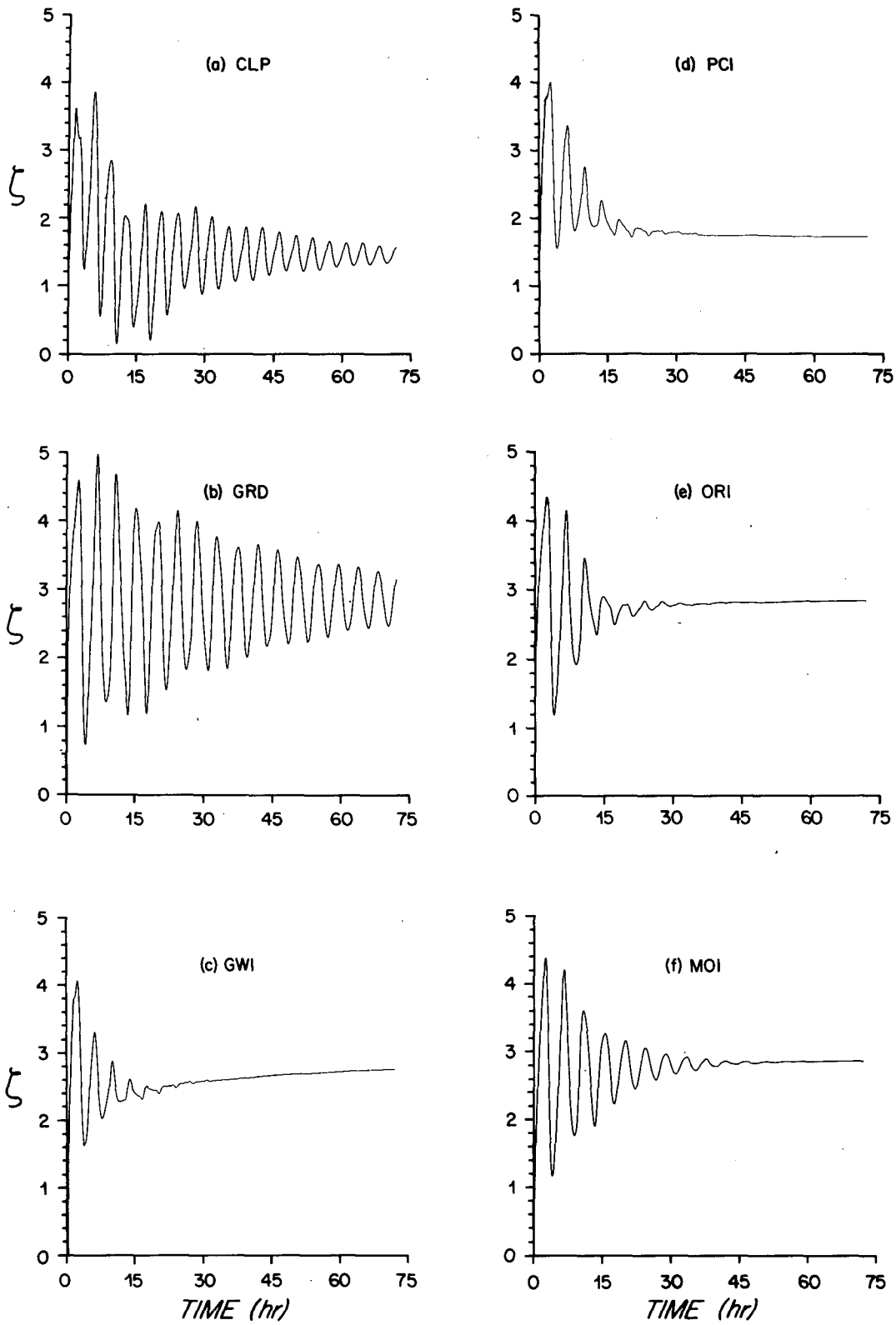

FIG. 7. Time history of sea-surface elevation (cm) at (x, y) = (80 km, −5 km) in the cross-shelf wind-stress experiment using (a) CLP, (b) GRD, (c) GWI, (d) PCI, (e) ORI, (f) MOI (τ_s^y = 1 dyn cm^{-2}, r = 0.05 cm s^{-1}, $f = 10^{-4}$ s^{-1}).

$$\zeta_{yy} + \frac{h_y}{h}\zeta_y + \left(\frac{\omega^2 - f^2}{gh}\right)\zeta = 0 \qquad (4.12)$$

for motions with frequency ω. Equation (4.12), along with boundary conditions (4.11b), has also been solved by a shooting technique [again using (4.1) for the topography] which yields $\omega = 3.84 \times 10^{-4}$ s^{-1} or a period of 4.54 hours. The observed period in Fig. 7b is 4.36 hours suggesting that the oscillations in Fig. 7b are due to the lowest mode seich (with the GRD conditions).

There are no true seiching modes when using the other OBCs, so the solutions quickly reach steady state. However, the steady-state sea surface elevations (ζ after 72 hours) vary with the different OBCs (Fig. 7, Table 2). The theoretical steady state may be approximated by neglecting time derivatives, x derivatives and cross-shelf bottom friction ($\tau_b^y = 0$) in (2.1). The resulting sea surface elevation is described by

$$\zeta_{yy} = \frac{-\tau_s^y}{\rho g}\frac{h_y}{h^2}. \qquad (4.13a)$$

Boundary conditions are

$$\zeta = 0 \quad \text{at} \quad y = -L$$

$$\zeta_y = \frac{\tau_s^y}{\rho g h_0} \quad \text{at} \quad y = 0. \qquad (4.13b)$$

Using $\tau_s^y = 1$ dyn cm^{-2} and the full form of h given by (4.1), then (4.13) may be integrated to yield

$$\zeta = \begin{cases} -2.55 \ln(300 - 0.0004y) + 18.86, \\ \qquad -5 \times 10^5 < y < 0 \\ -1.02 \ln(-0.001y) + 9.35, \\ \qquad -95 \times 10^5 < y < -5 \times 10^5 \\ -0.0054 \ln(-1.80025 \times 10^6 - 0.1905y) \\ + 0.065, \qquad y < -95 \times 10^5. \end{cases} \qquad (4.14)$$

The corresponding steady-state cross-shelf and alongshelf transports are zero everywhere.

The nearly constant values of ζ at $(x, y) = (80, -5)$ km approached after 72 hours in Fig. 7 are listed in Table 2 along with the theoretical value from (4.14). Cross-shelf profiles of ζ at $x = 70$ km after 72 hours are shown in Fig. 8a for each OBC along with the theoretical profile (solid curve) from (4.14). The steady states achieved with ORI, MOI and SPO are very close to the theoretical curve with SPO predictions falling virtually on the curve in Fig. 8a. The GRD steady state is close to the curve, but it is still oscillating due to the seiches. The GWI results underestimate the theoretical values as they did in the other experiments. Most notable, however, are the grossly incorrect steady states achieved using both CLP and PCI. Both of these OBCs inhibit the setup near the open boundaries thus limiting the interior setup as well. This is shown again in Fig. 8b where the cross-shelf profiles of alongshelf transport are plotted. The theoretical values are zero everywhere because the surface Ekman transport exactly cancels the bottom Ekman transport. Again ORI, MOI, SPO

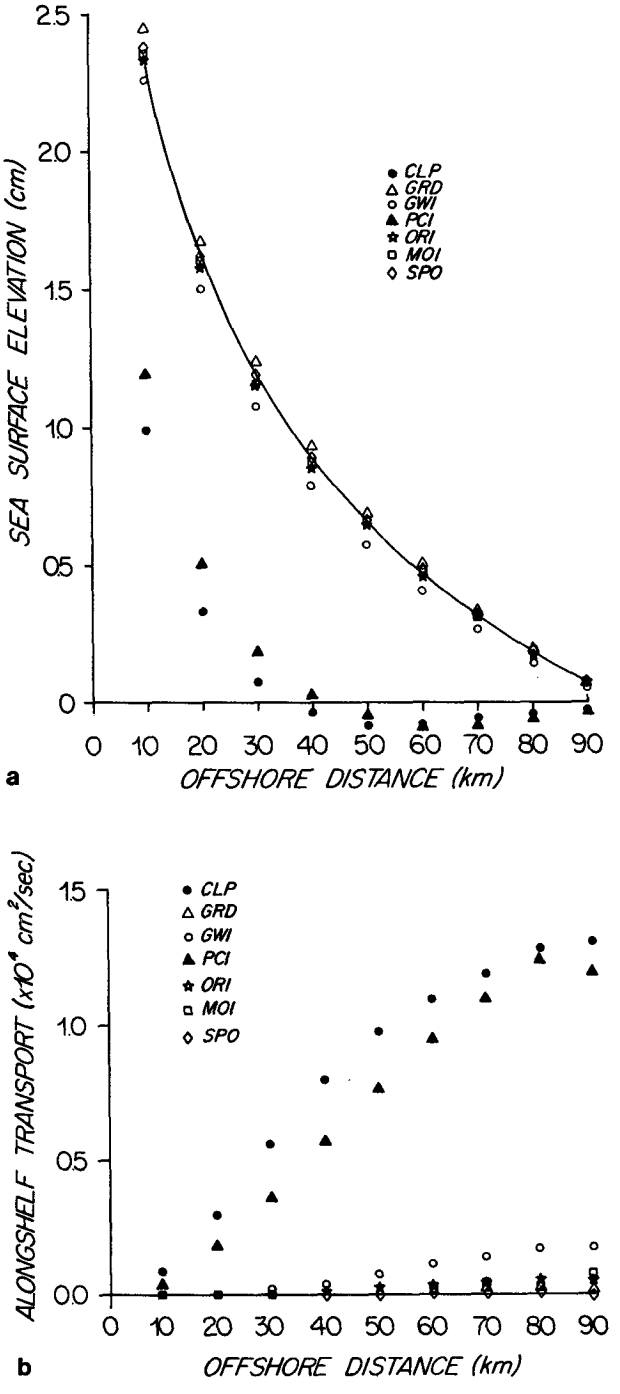

FIG. 8. Cross-shelf profiles of (a) sea-surface elevation and (b) alongshelf transport at $x = 70$ km after 72 h in the cross-shelf wind-stress experiment. Theoretical steady state is the solid curve in (a) and is identically zero in (b). Symbols identify the OBCs used ($\tau_s^y = 1$ dyn cm^{-2}, $r = 0.05$ cm s^{-1}, $f = 10^{-4}$ s^{-1}).

and GRD are close to zero, although GRD is oscillating substantially. The GWI results are somewhat less acceptable while the alongshelf transports using CLP and PCI are large over most of the shelf. The conclusion is that CLP and PCI are unacceptable for coastal numerical models which include a cross-shelf wind stress.

The clamped offshore boundary has a substantial effect on the response in this experiment. In some sense, the results using GRD may be the most accurate because the seiches *should* be present if the deep ocean has nearly infinite depth. On the other hand, the time scale of the seiches is fairly small—much less than the 2–10 day time scales of primary interest in large-scale wind-driven coastal models. Therefore, it can be argued that the "best" OBC for modelling a coastal wind-driven response is one which allows the rapid removal of the seiching, yet has the correct low-frequency response. Further, most realistic large-scale models have alongshelf variations in both bottom topography and coastline as well as nonuniform wind forcing, so that seiching should not be a serious problem. For these reasons, the ORI, MOI and SPO conditions are considered to perform in the most desirable fashion for the cross-shelf wind stress experiment.

5. Summary

Testing of OBC performance could continue indefinitely. For example, the effects of different bottom frictions, different topographies, time-dependent wind forcing as well as grid size, time step, treatment of the offshore open boundary, other OBCs and other finite-difference schemes could all be explored. Therefore, both the number of OBCs considered and the types of numerical experiments used to compare the OBCs must be limited. For this reason, the present set of OBCs and experiments is far from exhaustive. However, even these few experiments show that coastal flows can be drastically changed simply by using different OBCs. Thus, at the very least, the results should serve to emphasize the importance of OBCs in barotropic coastal models and to encourage the use of simple tests to compare various OBCs before choosing one.

The experiments performed here represent a cross section of the types of behavior with which an OBC in a barotropic coastal model might deal. Not every coastal model will include all of these behaviors, so it may be unfair to rank the OBCs based on total performance. For example, if a coastal model deals primarily with wave propagation and no wind forcing, then SPO is clearly the most accurate OBC. (And its performance could be improved by adjusting the sponge parameters.) But SPO did not fare well with alongshelf wind driving. Instead ORI and MOI appeared better suited for that problem. In other words, for a specialized problem, an OBC could probably be tailored to fit the desired behavior. On the other hand, if a barotropic coastal model is designed to study general flows over the shelf, then all of the behaviors may at some time be important. In this case, the recommended OBC (of those tested) is ORI (Orlanski radiation condition applied in implicit form) because its response is adequate in the barotropic relaxation experiment and entirely acceptable in the wind stress experiments. All other OBCs performed poorly in at least one of the experiments. It should be emphasized, however, that new OBCs continue to be developed (e.g., Roed and Smedstad, 1984), and such OBCs should be tested and compared with others to understand their relative strengths and weaknesses.

Finally, the present results suggest that any OBC which significantly clamps the cross-shelf open boundaries should be avoided. In particular, a clamped open boundary (CLP) is probably the worst choice of cross-shelf OBC for barotropic coastal models. It (i) is a perfect reflector of wave energy, (ii) severely limits the geostrophic flow through the open boundary, and (iii) prohibits the sea surface change associated with setup or setdown. Further, its effects may be important far from the open boundary (Section 4b) which then requires an enormous spatial domain in order to have any unaffected interior region.

Acknowledgments. I am indebted to R. C. Beardsley and D. B. Haidvogel for their encouragement and generosity in providing their barotropic coastal model for use and modification. Numerous discussions with D. Haidvogel proved enormously helpful. K. H. Brink and D. L. Musgrave provided valuable comments as well. This research was supported by the National Science Foundation under Grant OCE 80-14941.

APPENDIX

Edge Waves in the Numerical Grid

Edge waves probably represent the dominant form of large-scale transient motion in the present coastal model during most adjustment periods. Therefore, it is important that the numerical model resolve the dominant edge waves with reasonable accuracy. For example, if the grid spacing of 10 km is too large to resolve edge waves, then the model will not respond realistically and the effects of the various OBCs will be meaningless.

To examine the approximate behavior of free edge waves in the numerical grid, the finite-difference forms of (2.1) with no rotation ($f = 0$) and no bottom-friction ($r = 0$) can be combined and written as

$$\frac{\delta^2\zeta}{\delta t^2} - gh_{jm}\left(\frac{\delta^2\zeta}{\delta x^2} + \frac{\delta^2\zeta}{\delta y^2}\right) + gh_y\frac{\delta\zeta}{\delta y} = 0 \qquad \text{(A1)}$$

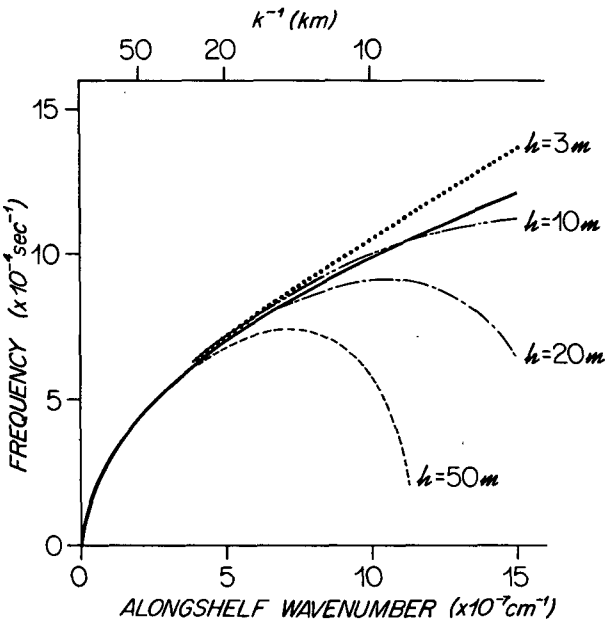

FIG. A1. Theoretical dispersion curve (solid) for the lowest mode edge wave with $h_y = -0.001$. Numerical dispersion curves (dashed) for the lowest mode edge wave given by (A3) with $h_y = -0.001$, $\Delta x = 10$ km, $\Delta t = 150$ sec, and various depths h_{jm}.

where $\delta^2/\delta t^2$, $\delta^2/\delta x^2$, $\delta^2/\delta y^2$, $\delta/\delta y$ represent centered second differences, h_{jm} the water depth at $x = j\Delta x$, $y = m\Delta y$, and h_y the cross-shelf bottom slope (assumed constant). The lowest mode edge wave on this grid should have the form

$$\zeta = Ae^{i\omega n\Delta t \pm ikj\Delta x + km\Delta y}, \qquad \text{(A2)}$$

i.e., propagating along the coast in either direction and decaying exponentially offshore. Substitution of (A2) into (A1) yields the numerical free-wave dispersion relation

$$\omega = \frac{1}{\Delta t}\cos^{-1}\left\{1 + gh_{jm}\frac{\Delta t^2}{\Delta x^2}[\cos(k\Delta x) + \cosh(k\Delta x) - 2] + gh_y\frac{\Delta t^2}{2\Delta x}\sinh(k\Delta x)\right\}. \qquad \text{(A3)}$$

For vanishingly small Δx and Δt, the exact dispersion relation, $\omega = (-g|k|h_y)^{1/2}$, is recovered. However, for nonzero (Δx, Δt) the dispersion relation (A3) is a function of y (due to h_{jm}), so that free edge waves do not really exist in the form (A2).

Figure A1 shows the exact dispersion curve along with solutions of (A3) for several choices of depth h_{jm} (with $\Delta x = 10$ km, $\Delta t = 150$ sec., $h_y = -0.001$). For small k ($<3 \times 10^{-7}$ cm^{-1}), the numerical solutions are indistinguishable from the exact solution independent of h_{jm}. As k increases, the difference between the exact and numerical dispersion curves becomes strongly dependent on h_{jm}. However, the "effective" h_{jm} in (A3) can be no larger than the maximum depth "felt" by the edge wave. In other words, only depths shoreward of the offshore decay scale (k^{-1}) can appreciably affect the wave dispersion. For example, with $h_y = -0.001$ a wave with offshore decay scale $k^{-1} = 20$ km ($k = 5 \times 10^{-7}$ cm^{-1}) can only be affected by depths $h_{jm} \leq 20$ m. The numerical dispersion curves for 3 m $\leq h_{jm} \leq$ 20 m are within 2 percent of the exact value at $k = 5 \times 10^{-7}$ cm^{-1} indicating that the term in (A3) involving h_{jm} is negligible. Similar examples with other wavenumbers suggest that the present numerical model should handle resolvable edge waves quite accurately.

REFERENCES

Beardsley, R. C., and D. B. Haidvogel, 1981: Model studies of the wind-driven transient circulation in the Middle Atlantic Bight. Part 1: Adiabatic boundary conditions. *J. Phys. Oceanogr.*, **11**, 355–375.

Bennett, A. F., and P. C. McIntosh, 1982: Open ocean modeling as an inverse problem: Tidal theory. *J. Phys. Oceanogr.*, **12**, 1004–1018.

Blumberg, A. F., and L. H. Kantha, 1982: A numerical model of the shelf circulation in the Middle Atlantic Bight driven by tides, transient storms and offshore large-scale circulation: Formulation of proper open boundary conditions. Dynalysis of Princeton Rep. No. 73, Princeton, NJ, 185 pp.

Camerlengo, A. L., and J. J. O'Brien, 1980: Open boundary conditions in rotating fluids. *J. Comput. Phys.*, **35**, 12–35.

Chen, J. H., 1973: Numerical boundary conditions and computational modes. *J. Comput. Phys.*, **13**, 522–535.

Csanady, G. T., 1978: The arrested topographic wave. *J. Phys. Oceanogr.*, **8**, 47–62.

Davies, H. C., 1983: Limitations of some common lateral boundary schemes used in regional NWP models. *Mon. Wea. Rev.*, **111**, 1002–1012.

Flagg, C. N., B. A. Magnell, D. Frye, J. J. Cura, S. E. McDowell and R. I. Scarlet, 1982: Interpretation of the physical oceanography of Georges Bank. EG & G Environmental Consultants, Waltham, MA. Final Rep. prepared for U.S. Dept. of Interior, Bureau of Land Management, 901 pp.

Israeli, M., and S. A. Orszag, 1981: Approximation of radiation boundary conditions. *J. Comput. Phys.*, **41**, 115–135.

Orlanski, I., 1976: A simple boundary condition for unbounded hyperbolic flows. *J. Comput. Phys.*, **21**, 251–269.

Roed, L. P., and O. M. Smedstad, 1984: Open boundary conditions for forced waves in a rotating fluid. *SIAM J. Sci. Stat. Comput.*, **5**, 414–426.

Wang, D.-P., 1982: Effects of continental slope on the mean shelf circulation. *J. Phys. Oceanogr.*, **12**, 1524–1526.